Abstract: We determine action dependent damping coefficients for electron coolers with cylindrical and hollow beams and action dependent diffusion coefficients from the interaction with a pellet target and a simple model of intrabeam scattering. We use these coefficients to numerically solve the time-dependent \FPE\ and present simulations of the transient cooling down. An efficient integrator makes it possible to simulate long times (hours) very efficiently and quickly. Moreover we determine a maximum acceptable limit of the cooling time to provide stable operation.

Transverse Profiles and Stability Limits with Electron Cooler and Pellet Target

V. Ziemann, Uppsala University

Abstract

We determine action dependent damping coefficients for electron coolers with cylindrical and hollow beams and action dependent diffusion coefficients from the interaction with a pellet target and a simple model of intrabeam scattering. We use these coefficients to numerically solve the time-dependent Fokker-Planck equation and present simulations of the transient cooling down. An efficient integrator makes it possible to simulate long times (hours) very efficiently and quickly. Moreover we determine a maximum acceptable limit of the cooling time to provide stable operation.

1 Introduction

The beam sizes and particle distributions in storage rings that are equipped with electron coolers and internal targets and operate at high beam intensities are determined by the competition of the friction force due to the electron cooler and the diffusion due to the target and intrabeam scattering (IBS). This is particularly important for cooler rings that will operate at luminosities in the $10^{32}/\mathrm{cm}^2\mathrm{s}$ range with 10^{11} particles per beam and targets with thickness in the $10^{15}/\mathrm{cm}^2$ range. These extreme conditions warrant a study of stability issues. The longitudinal dynamics was already investigated in Ref. [1] and [2] and in the latter report limits for stable operation in the longitudinal plane were determined. In this report we focus on the transverse direction and will discuss the profile of the distribution and the temporal evolution towards a quasi-equilibrium. Since all the processes involved act on a slow time scale long with respect to the revolution

---

frequency we can adopt a description that employs the phase-averaged Fokker-Planck equation that only depends on the transverse action variable J. In one dimension, the Fokker-Planck equation, we assume horizontal, is given by [3]

$$\frac{\partial \psi(J)}{\partial t} = \frac{\partial}{\partial J}\left(2\alpha J \psi(J) + DJ\frac{\partial \psi}{\partial J}\right) \tag{1}$$

where $\psi(J)$ is the sought distribution function. α is the damping coefficient and D is the diffusion coefficient. Both parameters potentially depend on the action variable J. The equilibrium distribution function is determined by setting the left hand side to zero. In the absence of a limiting aperture and for constant α and D we find the equilibrium distribution from Eq. 1 to be $\psi(J) = \exp(-J/\varepsilon)/\varepsilon$ with $\varepsilon = D/2\alpha$.

In real accelerators these simplifying assumptions are not given. There is always a limiting aperture in the form of the vacuum pipe causing losses, rendering the concept of a real equilibrium useless. Moreover, the damping coefficient α and diffusion coefficient D are in fact action-dependent. In particular the damping coefficient is strongly action-dependent, because particles with a large betatron action J often cross the electron cooler with a large angle and it is well-known that the cooling force strongly depends on the relative angle between electron and ion beam [4]. Therefore particles with large betatron action are less efficiently damped, and one can envision a scenario where cooling is insufficient to counteract the diffusion, leading to increased transport of particles into the tails and to increased losses. A second – often ignored – effect comes from the finite size of the electron beam. Particles with betatron amplitudes larger than the electron beam radius miss the electron beam on some turns, reducing the effective cooling rate further. A hollow beam is sometimes considered to match the ion beam size to the spacing between pellets to reduce the modulation of the luminosity [6]. It is also proposed [5] to counteract ultra-cold beam cores that lead to instabilities and increased electron capture. It will not cool the core at all and the tails at a reduced rate as will be discussed below. The diffusion coefficient from a gas or pellet target is also action dependent, because the target typically has a circular cross-section in the plane described by a vertical normal vector, i.e. looking from above. This causes the target to be thicker in the center leading to increased diffusion at small betatron action amplitudes. Moreover, large amplitude particles occasionally miss the target. Intrabeam scattering will aggravate the diffusion into the tails beyond that caused by the target. The interplay of these action dependent effects will determine the tranverse beam profile and the losses.

The detailed shape of the transverse distribution is of relevance for the nuclear physics experiments utilizing the interaction of the beam with the target, because an increased beam core size reduces the overlap between the beam and the target, thereby reducing the luminosity. Increased beam tail population and subsequent beam loss leads to worse background conditions that lead to reduced efficiencies

2

of the detector.

In order to describe the complex scenario of action dependent damping and diffusion together with a finite aperture we will calculate the respective coefficients for realistic targets and transverse electron cooler current profiles. Then we construct an efficient numerical algorithm to integrate the Fokker-Planck equation over very long time scales of hours which reveals the evolution of the distribution function. We use the simulation program to explore the ability of the cooler to counteract the diffusion caused by the target.

2 Cooler Overlap

We start by investigating the friction force due to the electron cooler where the damping constant α is given in terms of the cooling time τ by $\alpha = 1/\tau$. The action dependence of the cooling force can be described by

$$\alpha = \frac{1}{\tau} = \frac{1}{\tau_0} \frac{1}{(1 + J/J_0)^{3/2}} \tag{2}$$

with

$$\alpha_0 = \frac{1}{\tau_0} = \frac{4\pi Z^2 r_p r_e c n_e \eta_c L_c}{A \gamma^2} \left(\frac{c}{v_{\text{eff}}}\right)^3 \tag{3}$$

where r_p and r_e are protons and electrons classical radius, respectively and n_e is the electron density, L_c is the Coulomb log, v_{eff} is the effective velocity that represents the sum of all imperfections of the electron cooler, such as magnetic field misalignment or power supply ripple and is assumed to be on the order of 3×10^4 m/s. For J_0 we then have $4\,10^{-8}$ mrad. The action dependent reduction factor in Eq. 2 represents the reduction in cooling when the relative velocity of electrons and ions is large due to the large Courant-Snyder invariant J of the ion. In the remainder of this report we use α_0 as a parameterization of the 'strength' of the cooler.

The effect of finite transverse size of the electron beam, however, is not yet taken into account. An ion with large betatron amplitude $r = \sqrt{2\beta_c J}$ obviously spends a fraction of its time inside the electron beam and another fraction outside. In order to determine the distribution function we consider the distribution of a particle performing betatron oscillations. The projection of the ellipses in phase space onto the horizontal axis is obtained after integrating over the x' variable which, after normalization, results in the distribution function

$$\psi(x) = \frac{1}{\pi} \frac{1}{\sqrt{r^2 - x^2}} \ . \tag{4}$$

The probability of being in the electron beam is given by the overlap of the distribution given by Eq. 4 and the radial distribution function of the electron
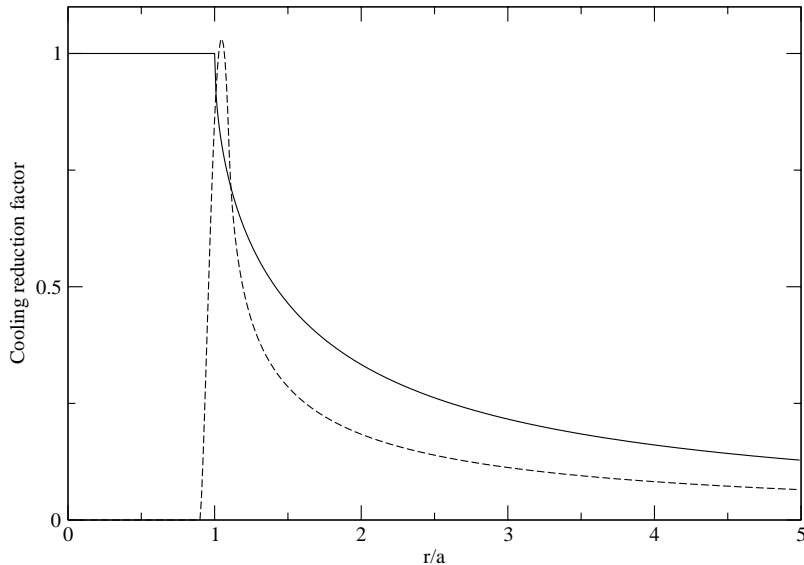
Figure 1: The reduction factor $R(r)$ as a function of the betatron amplitude $r = \sqrt{2\beta_c J}$ for a solid cylindrical electron beam (solid line) and for a hollow beam (dashed line).

beam. For a solid cylindrical electron beam with radius a this reduction factor $R(r)$ is given by the following overlap integral

$$R(r) = 2 \int_0^a \frac{1}{\pi} \frac{1}{\sqrt{r^2 - x^2}} dx = \begin{cases} 1 & \text{if } r < a \\ (2/\pi) \arcsin(a/r) & \text{if } r > a \end{cases} \tag{5}$$

We observe that the reduction factor is unity if the amplitude of the ion beam r is inside the electron beam, but reduced outside. The solid line in Fig. 1 shows the dependence of the reduction factor $R(r)$ on the amplitude r.

For an extreme hollow electron beam with a parabolic annular ring of radius b and width $2a = b/10$ the reduction factor $R_h(r)$ is given by

$$R_h(r) = 2 \int_{b-a}^{b+a} \frac{1}{\pi} \frac{1}{\sqrt{r^2 - x^2}} \frac{1}{N_0} \left[1 - \frac{(x-b)^2}{a^2} \right] dx \tag{6}$$

with the normalization constant $N_0 = 8\pi ab/3$. The integrals can be solved by elementary means using integrals number 164 to 166 in ref. [7] where we need to distinguish three cases: first $r < b - a$, second $b - a < r < b + a$, and third $b + a < r$. We display the resulting reduction factor by the dashed line in Fig. 1.

4

We observe that cooling is absent inside the hollow beam and that the reduction factor decays stronger at large amplitudes compared with the solid cylindrical beam. Already here it is obvious that a hollow electron beam cools considerably less than a cylindrical beam with the same electron current.

3 Target Overlap

The beam particles experience multiple transverse small-angle scattering in the target which causes transverse diffusion. The RMS transverse kick angle in a target of thickness $\bar{\rho}$ is given by [10]

$$\theta_{rms} = \frac{13.6 \, \text{MeV}}{\beta^2 E} \sqrt{\frac{\bar{\rho}}{X_0}} \tag{7}$$

where $X_0 = 3.77 \, 10^{25}/\text{cm}^2$ is the radiation length [10] of solid hydrogen and E is the energy of the ions. For $\bar{\rho}$ we assume the average thickness of $4 \, 10^{15}/\text{cm}^2$. The diffusion constant due to the average target thickness $\bar{D}$ is then given by

$$\bar{D} = \frac{\beta_t f_0}{2} \theta_{rms}^2 \tag{8}$$

where $\beta_t = 1 \, \text{m}$ is the beta function at the target and f_0 is the revolution frequency. The target has a circular distribution in the $x - z$ direction, characterized by the thickness $\rho(x)$ which is given by

$$\rho(x) = \frac{\pi \bar{\rho}}{2R} \sqrt{R^2 - x^2} \, . \tag{9}$$

The target thickness thus depends on the horizontal position x and correspondingly the diffusion constant will depend on the transverse position x as well. Note that the peak density $\hat{\rho}$ is related to the average density $\bar{\rho}$ by

$$\hat{\rho} = \frac{\pi}{2} \bar{\rho} \, . \tag{10}$$

In order to calculate the average over the betatron phases we have to average the target distribution $\rho(x)$ over the transverse distribution given by Eq. 4. We have to distinguish cases where the particle performs small oscillations and is completely embedded inside the target or that it performs large oscillations and sometimes misses the target. The relative geometry of the target and the beam performing small betatron oscillations is shown in dashes in Fig. 2. The case where the oscillation amplitude r is larger than the target radius R is shown as the dot-dashed line. The target is shown as the solid semi-circle in Fig. 2.

In order to calculate the effective target overlap we have to average the target distribution over the particle distribution and need to evaluate the following integral

$$I_{r<R} = \frac{1}{2R} \int_{-r}^{r} \frac{\sqrt{R^2 - x^2}}{\sqrt{r^2 - x^2}} \, dx \tag{11}$$
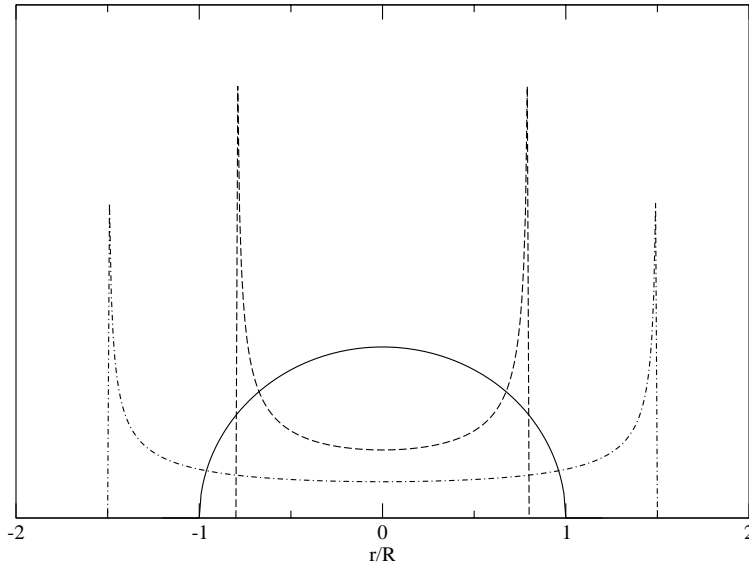
Figure 2: Betatron oscillations with amplitude less (dashed line) and larger (dot-dashed line) than the target with radius R, here shown as the solid circle.

which describes the overlap of the betatron oscillations and the target if the betatron oscillation amplitude is less than the target radius, as shown by the dashed distribution in Fig. 2. The integral is easily solved with the substitution $x = r \sin \phi$ leading to

$$I_{r<R} = \frac{1}{R} \int_0^{\pi/2} \sqrt{R^2 - r^2 \sin^2 \phi}\, d\phi = E(r/R) \qquad (12)$$

where $E(k)$ is the complete elliptic integral of the second kind [8]. Note that this is only valid if the betatron oscillation is completely immersed in the target with $r < R$.

If the betatron oscillations have an amplitude r larger than the target radius R the upper limit of the integral extends to an angle $\hat{\phi}$ given by $R = r \sin \hat{\phi}$ and we obtain

$$\begin{aligned} I_{r>R} &= \int_0^{\arcsin(R/r)} \sqrt{1 - (r^2/R^2) \sin^2 \phi}\, d\phi \\ &= E(\arcsin(R/r), r/R) \end{aligned} \qquad (13)$$

where $E(\phi, k)$ now is the incomplete elliptic integral of the second kind [8].

In order to visualize the effect of the circular target on the beam that performs betatron oscillations we plot the effective target thickness in units of the average
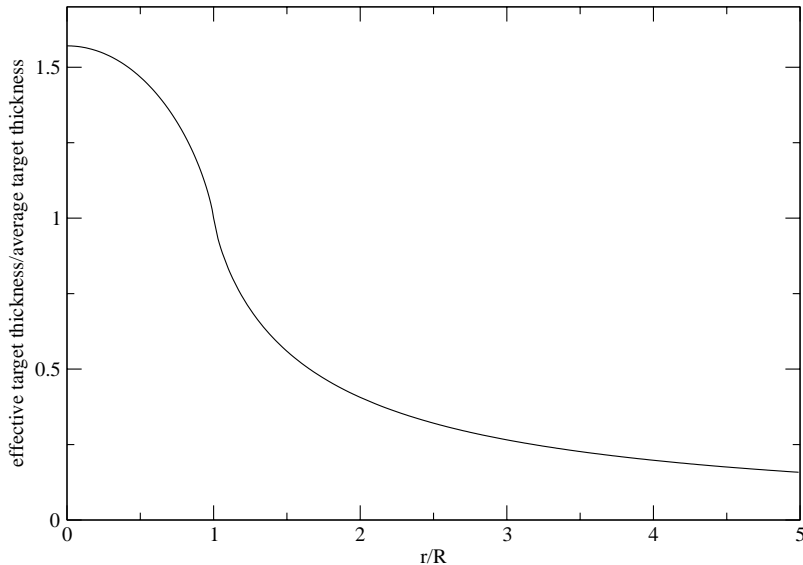
6

Figure 3: The effective target thickness as a function of the betatron oscillation amplitude $r = \sqrt{2J\beta}$. We use Eq. 12 for $r/R \leq 1$ and Eq. 13 for $r/R \geq 1$.

target thickness in Fig. 3 as a function of the betatron amplitude $r = \sqrt{2J\beta_t}$. Numerical routines to evaluate the elliptic integrals needed in the preparation of Fig. 3 can be found in reference [9]. Note that the effective target thickness is actually enhanced for particles with very small amplitude r, as can be expected from Eq. 10. If the betatron amplitude is equal to the target width, the target thickness that the ions experience is the average density $\bar{\rho}$ and for amplitudes larger than the target radius R the effective target thickness is reduced, because the ions pass through the target only a fraction of their turns.

4 Discretization of the Fokker-Planck Equation

The one-dimensional Fokker-Planck equation describing the dynamics of the betatron phase-averaged distribution function in the action variable J is given by

$$
\begin{aligned}
\frac{\partial \psi(J)}{\partial t} &= \frac{\partial}{\partial J}\left(2\alpha(J)J\psi(J) + D(J)J\frac{\partial \psi}{\partial J}\right) \\
&= \frac{\partial}{\partial J}\left(2\bar{\alpha}\psi(J) + \bar{D}\frac{\partial \psi}{\partial J}\right)
\end{aligned}
\tag{14}
$$

with the action dependent inverse damping time or damping coefficient $\alpha(J)$ and diffusion coefficient $D(J)$. In order to facilitate further manipulations we have introduced the abbreviations $\bar{\alpha} = J\alpha(J)$ and $\bar{D} = JD(J)$.

In case that we have constant α and D we can easily show that Eq. 14 is solved by the distribution

$$\psi_c(J) = \frac{1}{\varepsilon}e^{-J/\varepsilon} \tag{15}$$

with the emittance $\varepsilon = D/2\alpha$. We can prove that ε is really the emittance by calculating the average of J over the distribution function ψ_c

$$< J > = \int_0^\infty J\psi_c(J)dJ = \varepsilon \ . \tag{16}$$

This example will serve as a test to debug the numerical methods developed below.

Furthermore the distribution in action space can be related to that in real space by the integral transformation

$$\phi(x) = \frac{1}{\pi} \int_0^\infty \frac{\psi(J)}{\sqrt{2\beta J - x^2}}dJ \tag{17}$$

which is easily understood by observing that the integral is the weighted average of the distribution in action space ψ with the probability distribution Eq. 2 of a single particle with betatron amplitude $r = \sqrt{2\beta J}$. For the distribution $\psi_c(J)$ given by Eq. 15 the integral in Eq. 17 can be easily solved with the substitution $s = \sqrt{2\beta J - x^2}$. This leads to

$$\phi(x) = \frac{1}{\sqrt{2\pi\varepsilon\beta}} \exp\left[-\frac{x^2}{2\varepsilon\beta}\right] \tag{18}$$

which describes a centered Gaussian with RMS width $\sqrt{\varepsilon\beta}$, as expected.

In order to find the distribution function $\psi(J)$ that solves the Fokker-Planck equation Eq. 14 with action dependent damping and diffusion coefficients we will discretize the Fokker-Planck equation on a grid in action space with grid size Δx and provide an algorithm to calculate the distribution function after a time step Δt. The action in bin j is thus given by $J_j = (j-1)\Delta x$. To simplify the notation we introduce the quantity u_j^n which corresponds to the distribution function $\psi(J_j)$ at time step n. The simplest integrator is given by the forward-time step method and results in the following difference equation

$$
\begin{aligned}
\frac{u_j^{n+1} - u_j^n}{\Delta t} &= \left[\frac{\bar{\alpha}_{j+1}u_{j+1}^n - \bar{\alpha}_j u_j^n}{\Delta x} + \frac{\bar{\alpha}_j u_j^n - \bar{\alpha}_{j-1}u_{j-1}^n}{\Delta x}\right] \\
&\quad + \frac{1}{\Delta x}\left[\bar{D}_{j+1/2}\frac{u_{j+1}^n - u_j^n}{\Delta x} - \bar{D}_{j-1/2}\frac{u_j^n - u_{j-1}^n}{\Delta x}\right] \\
&= \frac{\bar{\alpha}_{j+1}u_{j+1}^n - \bar{\alpha}_{j-1}u_{j-1}^n}{\Delta x} \\
&\quad + \frac{\bar{D}_{j+1/2}(u_{j+1}^n - u_j^n) - \bar{D}_{j-1/2}(u_j^n - u_{j-1}^n)}{\Delta x^2} \ .
\end{aligned} \tag{19}
$$

8

where we introduced the diffusion term $\bar{D}_{j+1/2} = (\bar{D}_{j+1} + \bar{D}_j)/2$. It turns out that solving Eq. 19 for u_j^{n+1} in a straight-forward way is unstable [9] for large time steps Δt. A method to avoid this calamity is based on a trick called the Crank-Nicholson scheme which suggests to substitute the right-hand-side which depends on time step n by the average of that term at time step n and $n+1$. This trick makes the behavior stable even for large time steps Δt, albeit at the expense of having to deal with an implicit system of linear equations, because the sought functions u_j^{n+1} at time step $n+1$ now appear on both the left hand side and the right hand side of the equivalent of equation 19. The equation modified by the Crank-Nicholson method now reads

$$
\begin{aligned}
u_j^{n+1} - u_j^n = \ & \frac{\Delta t}{2} \left[\frac{\bar{\alpha}_{j+1} u_{j+1}^n - \bar{\alpha}_{j-1} u_{j-1}^n + \bar{\alpha}_{j+1} u_{j+1}^{n+1} - \bar{\alpha}_{j-1} u_{j-1}^{n+1}}{\Delta x} \right. \\
& + \frac{\bar{D}_{j+1/2}(u_{j+1}^n - u_j^n) - \bar{D}_{j-1/2}(u_j^n - u_{j-1}^n)}{\Delta x^2} \\
& \left. + \frac{\bar{D}_{j+1/2}(u_{j+1}^{n+1} - u_j^{n+1}) - \bar{D}_{j-1/2}(u_j^{n+1} - u_{j-1}^{n+1})}{\Delta x^2} \right] .
\end{aligned}
\tag{20}
$$

We now introduce scaled variables

$$
\tilde{\alpha} = \frac{\Delta t}{2\Delta x} \bar{\alpha}, \qquad \tilde{D} = \frac{\Delta t}{2\Delta x^2} \bar{D}
\tag{21}
$$

to facilitate the writing and rewrite Eq. 20 to collect all terms at time step $n+1$ on the left hand side

$$
\begin{aligned}
(1 + \tilde{D}_{j+1/2} + \tilde{D}_{j-1/2}) u_j^{n+1} &+ (\tilde{\alpha}_{j-1} + \tilde{D}_{j-1/2}) u_{j-1}^{n+1} - (\tilde{\alpha}_{j+1} + \tilde{D}_{j+1/2}) u_{j+1}^{n+1} \\
&= (1 - \tilde{D}_{j+1/2} - \tilde{D}_{j-1/2}) u_j^n - (\tilde{\alpha}_{j-1} - \tilde{D}_{j-1/2}) u_{j-1}^n + (\tilde{\alpha}_{j+1} + \tilde{D}_{j+1/2}) u_{j+1}^n .
\end{aligned}
\tag{22}
$$

Inspection of Eq. 22 reveals that we have to solve a tridiagonal linear system of equations, which is easily accomplished using the subroutine `tridag` from [9]. We note in passing that solving a tridiagonal system is proportional to the size N of the system, rather than N^3 as it would be for a straight matrix inversion. We thus arrive at a very fast and robust calculation of a single time step. The detailed algorithm is given as follows:

1. First we assume that $\alpha(J)$ and $D(J)$ are given or are already determined using the discussions in the first few sections of this report. We then need to calculate $\tilde{\alpha}_j$ and $\tilde{D}_j$ on a grid in action space with spacing Δx such that we have $J_j = (j-1)\Delta x$.

$$
\begin{aligned}
\tilde{\alpha}_j &= \frac{\Delta t}{2\Delta x} J_j \alpha(J_j) = (j-1)\frac{\Delta t}{2}\alpha(J_j) \\
\tilde{D}_j &= \frac{\Delta t}{2\Delta x^2} J_j D(J_j) = (j-1)\frac{\Delta t}{2\Delta x} D(J_j)
\end{aligned}
\tag{23}
$$

9

2. Second we need to prepare the vectors $\vec{a}, \vec{b}, \vec{c}$ representing the lower, central, and upper diagonal band in the equations 22 that need to be solved to find the distribution function at time step $n + 1$

$$
\begin{aligned}
a_j &= \tilde{\alpha}_{j-1} - \frac{1}{2}(\tilde{D}_{j-1} + \tilde{D}_j) & \text{for } j = 2, \ldots, N \\
b_j &= 1 + \frac{1}{2}(2\tilde{D}_j + \tilde{D}_{j-1} + \tilde{D}_{j+1}) & \text{for } j = 1, 2, \ldots, N \quad (24) \\
c_j &= -\tilde{\alpha}_{j+1} - \frac{1}{2}(\tilde{D}_j + \tilde{D}_{j+1}) & \text{for } j = 1, \ldots, N - 1
\end{aligned}
$$

3. In the third step we need to prepare the vectors $\vec{d}, \vec{e}, \vec{f}$ that represent the lower, central, and upper diagonal band in the right hand matrix in Eq. 22

$$
\begin{aligned}
d_j &= -\tilde{\alpha}_{j-1} + \frac{1}{2}(\tilde{D}_{j-1} + \tilde{D}_j) & \text{for } j = 2, \ldots, N \\
e_j &= 1 - \frac{1}{2}(2\tilde{D}_j + \tilde{D}_{j-1} + \tilde{D}_{j+1}) & \text{for } j = 1, 2, \ldots, N \quad (25) \\
f_j &= \tilde{\alpha}_{j+1} + \frac{1}{2}(\tilde{D}_j + \tilde{D}_{j+1}) & \text{for } j = 1, \ldots, N - 1
\end{aligned}
$$

4. In the next, fourth step we need to calculate the right hand side term r_j of Eq. 22 by multiplying the coefficients from Eq. 25 with the distribution u_j^n at time step n

$$
r_j = e_j u_j^n + d_j u_{j-1}^n + f_j u_{j+1}^n \qquad (26)
$$

where we assume that u_0^n and u_{N+1}^n are zero. This will also ascertain that losses at the aperture are treated correctly.

5. Substitute the vectors $\vec{a}, \vec{b}, \vec{c}$, and $\vec{r}$ into the routine `tridag` from ref. [9] to solve for the distribution function coefficients u_j^{n+1} in the next time step and display them.

6. Iterate item 4) and 5) to simulate the time-dependence of the system.

7. Iterating for a long time will drive the system to equilibrium. the time scale on which that happens depends of course on the cooling time.

It turns out that the algorithm is very stable and that very long time steps can be used. We simulated the dynamics of a system with constant damping time of $1000\,\mathrm{s}$ and diffusion over one damping time, namely $1000\,\mathrm{s}$. The initial distribution is chosen to have 10 times the emittance of the equilibrium beam. We then simulate the process by iterating $10 \times 100\,\mathrm{s}$, $100 \times 10\,\mathrm{s}$ and $1000 \times 1\,\mathrm{s}$ but found no visual difference in the distributions when plotting them on the same graph. Closer inspection reveals that the difference between the three curves is less than 10^{-5} where the $1000 \times 1\,\mathrm{s}$ and the $100 \times 10\,\mathrm{s}$ distributions are very

close. Comparing the simulated distributions after 10 damping times to the analytically calculated exponential equilibrium distribution shows differences on the same order of magnitude. We conclude that the algorithm works very well, even for large time steps.

5 Intrabeam Scattering

Intrabeam scattering describes the emittance growth due to Rutherford scattering events among the ions within the ion beam itself. In a denser beam, the probability of such events is larger. In this sense it can be described by an additional diffusion term with an emittance dependent magnitude. In ref. [1] it is shown that this diffusion term for the horizontal plane can be written as

$$D_{ibs} \approx \frac{1}{2} \Big\langle \frac{\eta_x^2}{\bar{\beta}_x} \Big\rangle \frac{\Lambda_\parallel}{\varepsilon^{3/2}} \tag{27}$$

where the longitudinal diffusion term is given by

$$\Lambda_\parallel = \frac{\sqrt{\pi} N c r_i L_c}{4 \gamma^3 \beta^3 C \sqrt{\bar{\beta}}} \ . \tag{28}$$

and $\bar{\beta}$ is the average beta function, C is the circumference, r_i the classical ion radius, L_c the coulomb radius and N the number of ions. For numerical values we follow Table 2 of Ref. [1]. Note that this method only gives an average diffusion for all particles in the ion beam independent of their betatron amplitude, whereas in reality one would expect a larger diffusion rate in the core where the density and the collision probability is high.

In the simulation program we included intrabeam scattering in the simple semi-self-consistent form described in the previous paragraph by calculating the RMS emittance after each time step and using it to calculate new diffusion constants $\tilde{D}(J_j)$ and updating the arrays $\vec{a}, \ldots, \vec{f}$ in Eq. 24 and 25 before the subsequent iteration.

6 Simulations

In order to simulate the transverse beam dynamics in the HESR under realistic conditions we have chosen the grid in action space to have $20\,000$ grid locations with a grid spacing of $2.5\,10^{-9}$ m-rad. This allows to investigate small emittances below 10^{-8} m-rad and also losses due to the limited vacuum chamber radius in the detector $r = \sqrt{2\beta_t J_{max}} = 0.01\,\text{m}$ where we assume $\beta_t = 1\,\text{m}$ and $J_{max} = 5\,10^{-5}$ mrad. The beam kinetic energy T in the simulation is $T = 4000\,\text{MeV}$. The cooler is located at a location with $\beta_c = 100\,\text{m}$ beta function and the electron beam has a radius of $r_c = 5\,\text{mm}$ which corresponds to the action
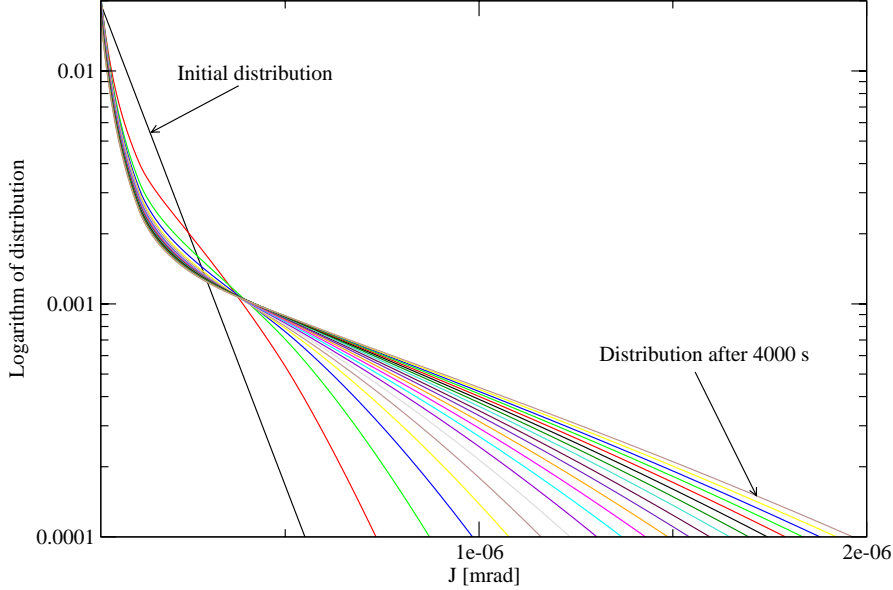
Figure 4: The distributions in action space over a period of $4000\,\mathrm{s}$ with $200\,\mathrm{s}$ between profiles for $\alpha_0 = 0.01/\mathrm{s}$.

$J_r = r_c^2/2\beta_c = 1.25\,10^{-7}\,\mathrm{mrad}$. For the transverse effective velocity v_{eff} we assume $v_{\mathrm{eff}} = 3\,10^4\,\mathrm{m/s}$. This results in the action variable $J_0 = 4\,10^{-8}\,\mathrm{mrad}$ which describes the dependence of the cooling time on the emittance in Eq. 2. As initial distribution we always choose a Gaussian with emittance $\varepsilon = 10^{-7}\,\mathrm{mrad}$. The target has a width of $\pm 1\,\mathrm{mm}$ with an average density $\bar{\rho} = 4\,10^{15}\,/\mathrm{cm}^2$ which results in an average diffusion constant of $\bar{D} = 2.3\,10^{-10}\,\mathrm{m/s}$.

In the first simulation we use a damping decrement of $\alpha_0 = 0.01\,\mathrm{s}$ which corresponds to a small-amplitude damping time of $\tau_0 = 100\,\mathrm{s}$ and use an integration time of 20 for a total simulation time of $4000\,\mathrm{s}$, a little over one hour. Such a run takes less than a minute of CPU time on a reasonably modern PC. In Fig. 4 we display the evolution of the distribution in action space $\psi(J)$ on a logarithmic scale as a function of J for 20 intervals with $200\,\mathrm{s}$ inbetween, i.e. plotted after every 10 consecutive iterations. The horizontal axis is restricted to $J < 2\,10^{-6}\,\mathrm{mrad}$ rather than the maximum J_{max} used in the simulations in order to improve the visibility of relevant features of the distributions. We see that the initial Gaussian distribution is cooled down to in the center while simultaneously developing tails at larger action values to the right. Note that the equilibrium emittance for this situation were $\varepsilon_0 = D/2\alpha = 1.15\,10^{-8}\,\mathrm{mrad}$ if cooling and diffusion operated
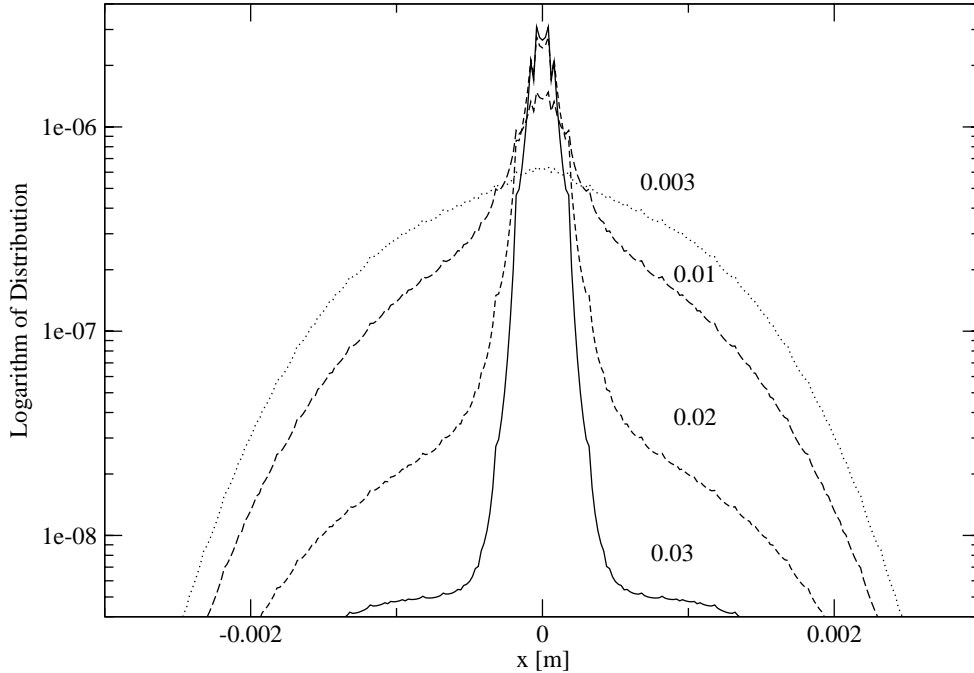
Figure 5: Distributions after $4000\,\mathrm{s}$ for $\alpha_0 = 0.003, 0.01, 0.02, 0.03/\mathrm{s}$.

homogeneously and independent of J. Here, however, their action dependence causes tails to grow. Note that the simulation runs for at least 13 damping times and still the equilibrium is not reached.

To obtain an impression how the final profiles after $4000\,\mathrm{s}$ look like in real space we use Eq. 17 and display the final profiles in Fig. 5 for $\alpha_0 = 0.003$, 0.01, 0.02, $0.03/\mathrm{s}$ corresponding to small-amplitude cooling times between $33\,\mathrm{s}$ and $333\,\mathrm{s}$. The slight raggedness of the curves is a result of the numerical integration in Eq. 17 when converting the distribution function in action variables to the projection in real space. We observe a narrow core of the distribution and tails that progressively become more pronounced as the damping decrement is decreased. It appears that there is a distinct change between $\alpha_0 = 0.01$ and $\alpha_0 = 0.02$ where a small change in the damping decrement changes the magnitude of the tails by a big amount.

In order to investigate this qualitative change further we display the emittance that is calculated using Eq. 16 as a function of time and show the result in Fig. 6.
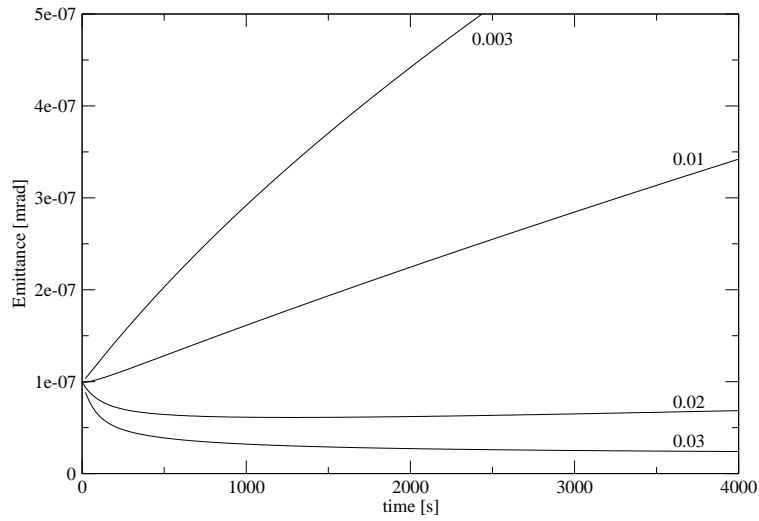
13

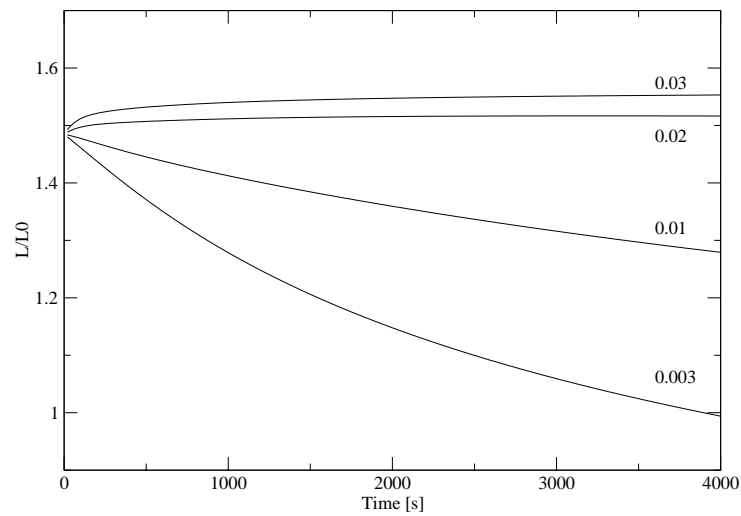Figure 6: The emittance as a function of time for different values of α_0.

Figure 7: The relative luminosity as a function of time for different values of the damping decrement α_0.
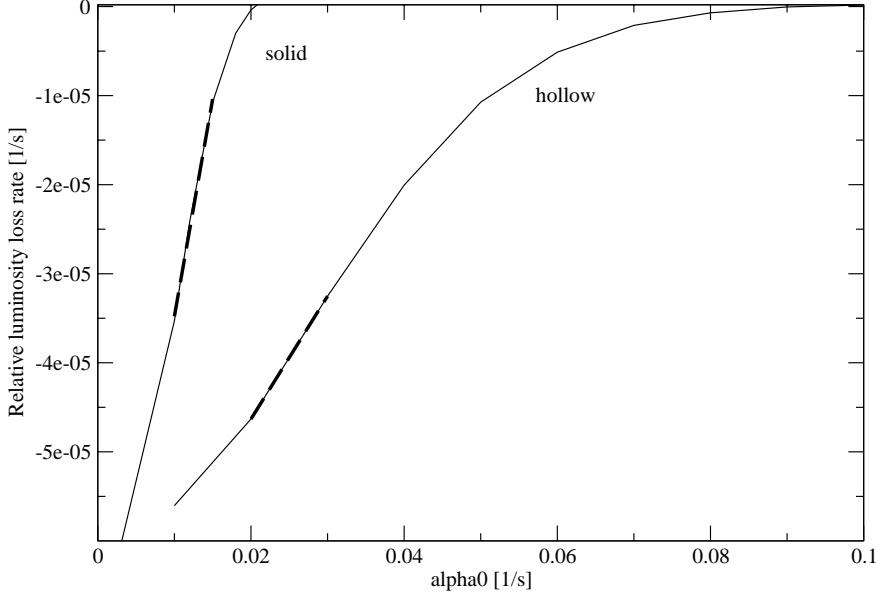
Figure 8: The luminosity loss rate after $4000\,\mathrm{s}$ as a function of the damping decrement α_0. The left curve is the loss rate for the solid cylindrical electron beam and the thick dashed line is a linear fit that intersects the $x-$axis at $\alpha_0 = 0.017$. The curve labeled 'hollow' is the loss rate for a hollow beam and the corresponding fit which intersects the $x-$axis at $\alpha_0 = 0.053$.

We observe that the emittance for $\alpha_0 = 0.03$ and $\alpha_0 = 0.02$ decreases as a function of time and approaches a finite equilibrium value whereas for smaller $\alpha_0 = 0.003$ and 0.01 the emittance continues to grow after $4000\,\mathrm{s}$. In Fig. 7 we show the corresponding time-evolution of the relative luminosity $\lambda = \mathcal{L}/\mathcal{L}_0 = \int \psi(J)I(J)dJ$, as a function of time. Here I is the function depicted in Fig. 3 and $\mathcal{L}_0$ is the average luminosity corresponding to all beam particles experiencing a target of thickness $\bar{\rho}$. Note that for strongly cooled beams the value approaches the peak value between average and peak luminosity $\pi/2$ as shown in Eq. 10. The explanation for this is that most of the beam is located in the center of the circular target distribution and therefore experiences the peak target thickness. In the simulation we also record the total beam current as the integral of the distribution, but found that it only changed by less than 10^{-4} in all simulations discussed above. We therefore did not loose beam at the aperture and the loss of luminosity is actually a consequence of the reduced target overlap and the correspondingly increased sampling of the target where it is less thick or missing
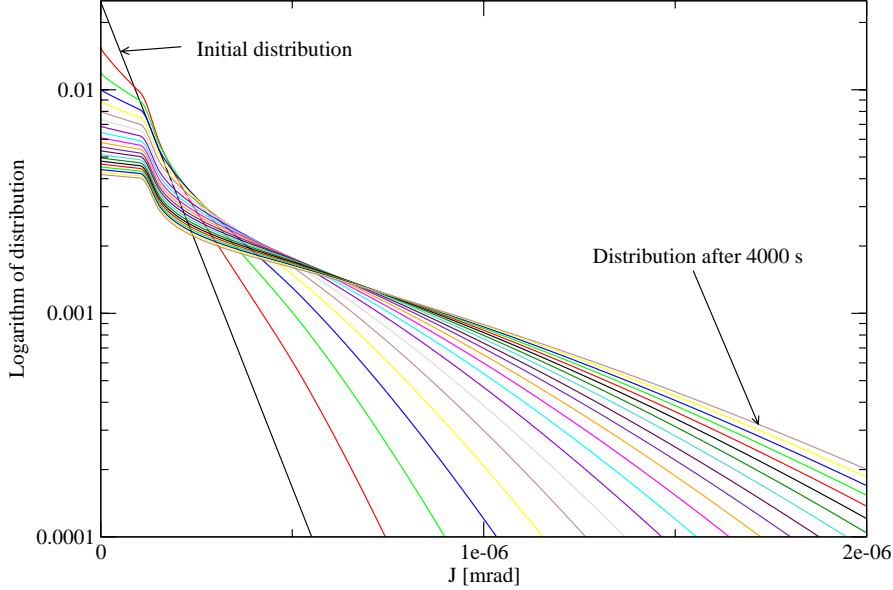
Figure 9: The distributions in action space over a period of $4000\,\mathrm{s}$ with $200\,\mathrm{s}$ between profiles for $\alpha_0 = 0.01/\mathrm{s}$ when cooling with a hollow electron beam.

it altogether.

We now investigate the qualitative change from damping to undamped behavior by plotting the time-derivative of the relative luminosity $d\lambda/dt$ after $4000\,\mathrm{s}$ as a function of the damping decrement α_0 in Fig. 8. We use the luminosity rather than the emittance, because the determination of the emittance as a RMS quantity is biased by strong tails and the luminosity is, after all, the quantity that is most relevant for the experiments. We observe that $d\lambda/dt$ is close to zero for large α_0 down to $\alpha_0 \approx 0.017$ where $d\lambda/dt$ abruptly starts to acquire significant non-zero values towards smaller values of α_0. We determine the cross-over value by the intersection of a linear fit indicated by the thick dashed line in Fig. 8 with the x-axis. The abrupt variation indicates a qualitative change in the behavior of the distribution, resembling a phase transition. This indicates that a cooler for the conditions stated above must at least provide cooling times below approximately 60 seconds in order to guarantee stable operation. In order to ensure that the observed threshold is not an artefact of a time range that is too small we repeated the calculation of the threshold with a ten-fold increased time range to $40000\,\mathrm{s}$ (half a day in real time) and found the same threshold.

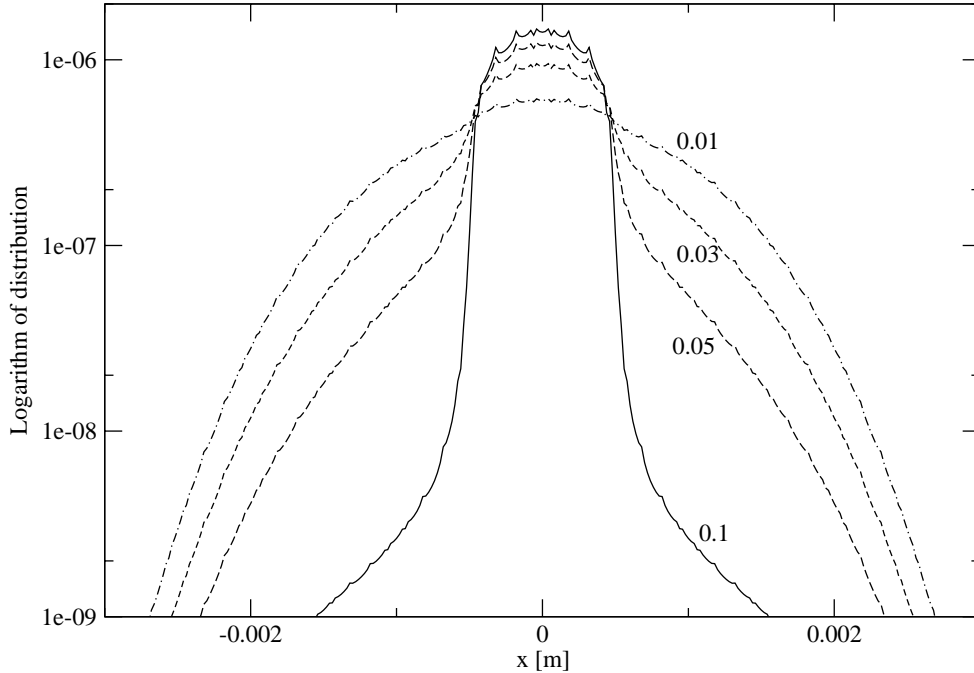We now turn to the investigation of hollow electron beams which are intro-

Figure 10: Distributions after $4000\,\mathrm{s}$ for $\alpha_0 = 0.01, 0.03, 0.05, 0.1/\mathrm{s}$ when cooling with a hollow electron beam.

duced in order to avoid excessive cooling of the core which leads to increased coherent instabilities such as self-bunching and also reduces losses due to electronic recombination, even though the latter is of no concern in an anti-proton accelerator. In the simulation the hollow beam is implemented by using the reduction factor $R_h(r)$ of the cooling for hollow electron beam in Eq. 6 instead of $R(r)$ for solid round electron beams in Eq. 5.

We start the investigation of the hollow beam by using the same damping decrement $\alpha_0 = 0.01/\mathrm{s}$ which led to Fig. 4 and show the corresponding time evolution of the profiles in Fig. 9. There we observe that the tails are growing more rapidly compared to Fig. 4. This is not surprising, because we saw in Fig. 1 that the reduction factor for hollow electron beam R_r which is shown as dashed line in Fig. 1 lies below that one for solid electron beam R which is shown by the solid line in Fig. 1. Obviously even large amplitude ions spend less time in the hollow electron beam compared to a scenario with a solid electron beam. In
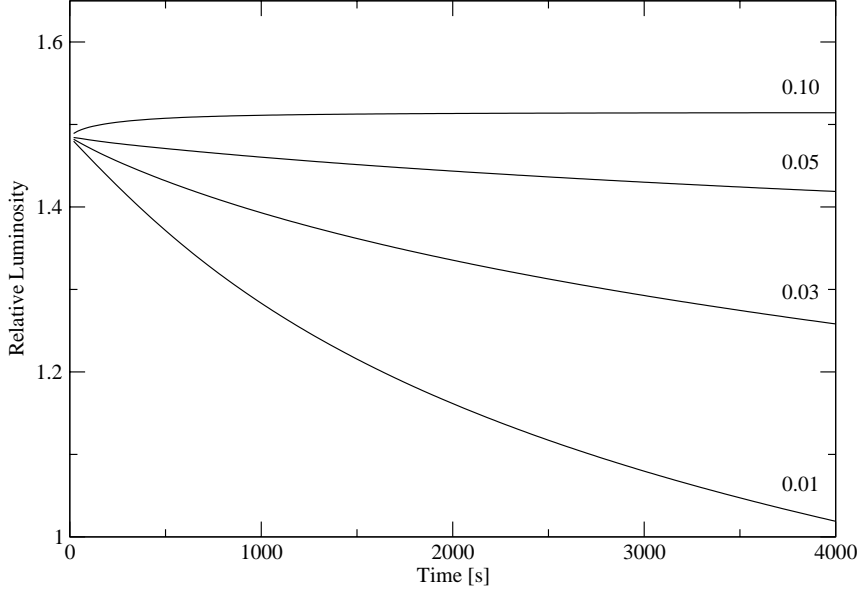
17

Figure 11: The relative luminosity as a function of time when cooling with a hollow electron beam for different values of α_0.

Fig. 9 we also observe that the hollow beam has the desired property to achieve a flat distribution near the origin, where a fraction of the ion beam is inside the hollow electron beam and experiences no cooling force. This is also clearly visible in Fig. 10 where we display the profiles after $4000\,\mathrm{s}$ for $\alpha_0 = 0.01$, 0.03, 0.05, and $0.1/\mathrm{s}$. For the larger values the beam is well-contained, but for values below 0.1 pronounced tails appear. This plot should be compared to Fig. 5 where large tails only appear for values of α_0 below $0.02/\mathrm{s}$.

We proceed by observing the relative luminosity as a function of time and display it for α_0 being varied between 0.1 and $0.01/\mathrm{s}$ in Fig. 11. We observe that the luminosity loss rate at $4000\,\mathrm{s}$ is only flat for $\alpha_0 = 0.1/\mathrm{s}$. Towards the right in Fig. 8 we plot the relative luminosity loss rate for the hollow beam in the same way we did for the solid electron beam. Making a linear fit to the curve, we find that it intersects the $x-$axis at $\alpha_0 \approx 0.053$, about three times the threshold value for solid electron beam. We conclude that a hollow electron beam shows considerably reduced capability to contain large amplitude particles. This will likely lead to increased background rates that will disturb the experiments.

Finally, we investigate the influence of IBS on the temporal evolution of the distributions and the luminosity. Since IBS is important mostly in high intensity
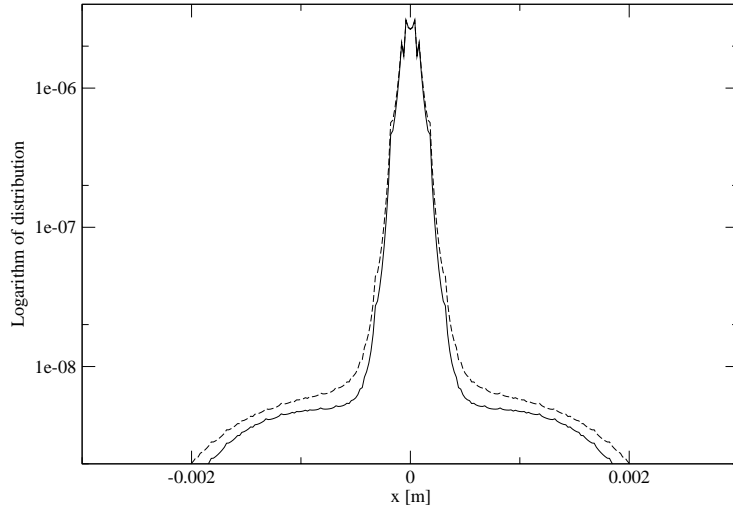
Figure 12: The profile after $4000\,$s with IBS (dashed line) and without IBS (solid line) with $\alpha_0 = 0.03/$s.
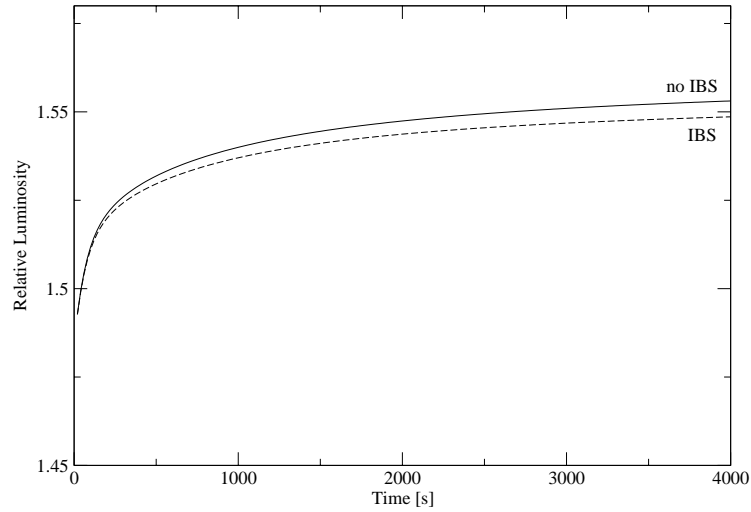

Figure 13: The relative luminosity as a function of time with IBS (dashed line) and without IBS (solid line). Note the suppressed zero of the vertical axis.

and very narrow beams, we can focus on the case with solid electron beams and strong cooling with $\alpha_0 = 0.03$/s. We assume that there are 10^{11} particles in the HESR ring and in this case the IBS diffusion constant D_{ibs} at emittance $\varepsilon_0 = 10^{-8}$ mrad is found to be $\hat{D}_{ibs} = 2.2\,10^{-10}$ m/s if we use the values from Table 2 in Ref. [1]. The diffusion constant for other emittances are found from scaling $\hat{D}_{ibs}$ with $(\varepsilon_0/\varepsilon)^{3/2}$.

In Fig. 12 we compare the profile after 4000 s with IBS taken into account to that without IBS which is the same as the curve labeled 0.03 in Fig. 5. We find that the influence of IBS is rather limited, which we attribute to the relatively high energy used in the simulations. The weak effect of IBS is also visible in the evolution of the relative luminosity. We compare the case with IBS to that without in Fig. 13 and find a very moderate increase of the emittance after 4000 s, on the order of a percent. The emittances after 4000 s calculated by Eq. 16 differ by about $30\,\%$ which shows that the tails play a dominant role in the determination of the RMS emittance, but play only a moderate role for the luminosity.

7 Conclusions

We calculated the action dependent damping coefficients of electron coolers for both solid and hollow electron beams. Moreover we determined the action dependent diffusion coefficients for a target that resembles a pellet target. The damping and diffusion constants are then used as input for the phase averaged Fokker-Planck equation to calculate the time evolution of the distribution function in action variables. The Fokker-Planck equation is solved using a fast and robust Crank-Nicholson solver. IBS is included in the model in a simple way by recomputing the IBS-diffusion constant periodically during a simulation run. The choice of simulating the distribution in action variables J allows to explore the small-scale variations of the distribution function below the 10^{-8} mrad scale as well as taking the aperture limit which is responsible for losses into account. Therefore both the core of the distribution which determines the luminosity and the tails, which determine background, are faithfully accounted for.

The resulting program was used to determine the limiting cooling time required to provide stable operation which is documented in the transition to non-zero-values of the relative luminosity loss rate in Fig. 8. This is the limit when the cooler becomes insufficient to contain the beam. Furthermore, we investigated how a hollow beam electron cooler performed and found that it cools especially large amplitude ions considerably less and much stronger coolers are required to contain the beam tails as well as a cooler with solid electron beam. The effect of IBS for the scenario investigated was found to be rather small.

The simulation program is rather fast. Simulating an hour of real time takes considerably less than a minute due to the fact that large integration time steps

can be taken because the Crank-Nicholson algorithm is numerically very stable. The speed allows to make extensive parameter scans in a reasonable time, which is deferred to later reports. In this report we have not utilized the capabilities of the code to investigate losses and potential background issues, which is also planned for the future. The code is only one-dimensional, focusing on the horizontal dimensions and extending to both transverse dimensions is desirable.

References

[1] O. Boine-Frankenheim, et.al. *Cooling equilibrium and beam loss with internal targets in the High Energy Storage Ring (HESR),* Nucl. Inst and Methods A 568 (2006) 475.

[2] V. Ziemann, *When are Pellets too thick?* Nucl. Inst. and Methods A 565 (2006) 370.

[3] D. Edwards, J. Syphers, *An introduction to the physics of high energy accelerators,* Wiley, New York, 1993.

[4] H. Poth, *Electron cooling: theory, experiment, application,* Physics Reports 196, 1990, 135.

[5] E. Behtenev, et.al., *Commission of Electron Cooler EC-300 for HIRFL-CSR,* Proceedings of the European Particle Accelerator Conference in Lucerne, July 2004.

[6] V. Ziemann, *On Pellet Target Luminosity Modulation,* Nucl. Inst. and Methods A 556 (2006) 641.

[7] I. Bronstein, K. Semendjajew, *Taschenbuch der Mathematik,* Verlag Harri Deutsch, Frankfurt, 1979.

[8] M. Abramowitz, I. Stegun, *Handbook of Mathematical Functions,* Dover Publications, New York, 1970.

[9] W. Press, et al., *Numerical Recipes,* Cambridge University Press, Cambridge, 1986.

[10] W.-M. Yao et al., *Review of Particle Physics,* J. Phys. G 33, (2006) 1, available online at `pdg.lbl.gov`.